A&A, 707, A94 (2026)
https://doi.org/10.1051/0004-6361/202557933

Astronomy & Astrophysics

The origin of sinusoidal brightness variations in F- to O-type stars through radial velocities

E. Šipková[1,2,⋆], M. Skarka[3], M. Vaňko[4], V. Chmelař[1], T. Pribulla[4], and Z. Mikulášek[1]

[1] Department of Theoretical Physics and Astrophysics, Masaryk University, Kotlářská 2, 61137 Brno, Czech Republic
[2] Institute of Astronomy, KU Leuven, Celestijnenlaan 200D, 3001 Leuven, Belgium
[3] Astronomical Institute of the Czech Academy of Sciences, Fričova 298, 25165 Ondřejov, Czech Republic
[4] Astronomical Institute of the Slovak Academy of Sciences, 059 60 Tatranská Lomnica, Slovak Republic

Received 31 October 2025 / Accepted 21 December 2025

ABSTRACT

Context. Stellar variability may originate from various phenomena such as binarity, pulsations, or rotation. These mechanisms can induce flux variations of similar magnitudes, shapes, and periods.
Aims. We aim to determine mechanisms responsible for the sinusoidal variations in main-sequence stars hotter than 6500 K.
Methods. We conducted our analysis using TESS long-cadence data complemented with high-resolution spectra from three spectrographs. From the initial sample of almost 46 000 objects, we selected 35 targets for spectroscopic follow-up. The comparison of light curves and radial-velocity curves allowed for the robust classification of these targets.
Results. Among the 35 selected objects, 18 displayed variability, suggesting the presence of a companion (including the discovery of seven new binary systems and one candidate for a triple-star system), one was identified as a new pulsator, nine as new candidates for spotted stars, and seven objects had uncertain classification. Our analysis shows that at least half of randomly selected stars with sinusoidal brightness variations are binaries.
Conclusions. The presented results illustrate the need for an individual approach to stellar classification, especially in cases where the photometric data alone is insufficient for determining the underlying phenomena behind the observed variations.

Key words. methods: data analysis – binaries: spectroscopic – stars: chemically peculiar – stars: rotation – stars: variables: general

1. Introduction

Various astrophysical processes can induce photometric variations, which may result in sudden, non-periodic, or quasi-periodic brightenings or periodic patterns. Periodic variations can be attributed to eclipses, pulsation, rotation, or other conditions and processes (e.g. Fetherolf et al. 2023). Understanding their origin is crucial for obtaining information about the dynamics, internal structure, and other fundamental properties of these objects (Kurtz 2022).

There have been several attempts to classify variable objects into distinct categories based on shared properties, for example, an updated version of Pickering's classification (Townley 1913) or classification in the General Catalog of Variable Stars (GCVS; Samus et al. 2017). Although such classifications are useful, transitions between classes can be continuous (Eyer & Mowlavi 2008), and the properties may overlap between different categories, making it difficult to identify the source of variability without additional information (e.g. spectra and observations in different wavebands; Skarka et al. 2022).

This work utilised the classification first proposed by Eyer & Mowlavi (2008) and revised in Eyer et al. (2018), which has been widely used in large-scale surveys, such as Gaia DR2 (Gaia Collaboration 2019) and WISE (Petrosky et al. 2021). This classification employs four levels of division. The first level distinguishes between the variability caused by intrinsic and extrinsic processes. The second level groups objects according to their type (asteroids, stars, active galactic nuclei), which are further divided according to the mechanism responsible for the variability. At last, objects with similar photometric properties, such as period, amplitude, timescale, and the shape of the light curve, are gathered in the last level of division (Eyer & Mowlavi 2008).

In our study, we focused on variable hot main-sequence stars with spectral classes of F-O. The most massive and luminous stars are valuable probes of stellar formation and galactic structure due to their short life spans, strong winds, and rapid evolution (e.g. Zinnecker & Yorke 2007; Marchant & Bodensteiner 2024; Eldridge & Stanway 2022). Stars of F-O spectral types are also useful for our understanding of the internal structure of stars, mixing processes, rotation, and angular-momentum transfer by interpreting their oscillations (see, e.g. reviews by Aerts et al. 2019; Aerts 2021; Kurtz 2022; Aerts & Tkachenko 2024). In general, hot stars[1] can be characterised by radiative outer layers and an absence of activity connected with convection, although some recent investigations show that there might be effects similar to those observed in cool stars present in hot stars. For example, Henriksen et al. (2023) and Antoci et al. (2025) found that rotational modulation in some hot stars is likely induced by spots of higher or lower temperature and sub-surface convection.

The rotation of F-O stars spans from slow to fast rotators (see, e.g. Royer et al. 2007). In stars where the mixing processes are negligible, typically stars with equatorial rotation velocities less than about 100 $\mathrm{km\,s^{-1}}$ (Mathys 2004; Abt & Morrell 1995; Qin et al. 2021), we often observe unusual chemical composition

⋆ Corresponding author: ema.sipkova@kuleuven.be

[1] Stars hotter than ≈ 6250 K (Kraft 1967).

and, thus, chemical peculiarity (CP; Maury & Pickering 1897; Preston 1974; Schnell 2008). Currently, we know tens of thousands of CP stars of various types (e.g. Ghazaryan et al. 2018; Lu et al. 2025). It is generally accepted that the CP phenomenon is a product of atomic diffusion in calm atmospheres when elements with large cross-sections are elevated to the surface layers, while elements with small cross-sections settle down (Michaud 1970; Michaud et al. 1976).

These elements can create spots that may be long-living and stabilised by a strong, globally organised magnetic field, forming a class of magnetic, chemically peculiar stars (mCP or Ap/Bp) stars (Preston 1974; Alecian 2015). The mCP stars are characterised by the overabundance of Si, Cr, Fe, Sr, and rare-earth elements (Preston 1974). The magnetic fields in mCP stars can be very strong, even reaching the order of tens of kilogauss (Babcock 1960; Bagnulo 2003; Shultz et al. 2019) and stable over decades (e.g. Donati & Landstreet 2009; Oksala et al. 2012; Shultz et al. 2018). The incidence rate of mCP stars among F-O stars is less than about 10% (Donati & Landstreet 2009; Sikora et al. 2019b). The origin of the magnetic field in hot stars without outer convective zones is assumed to be of a fossil nature surviving from the time of their formation via cloud collapse, or mergers (see, e.g.Braithwaite & Spruit 2004, Ferrario 2018, and Schneider et al. 2019). The impact of strong magnetic fields on stellar evolution, rotation, diffusion processes, and mass loss is still not fully understood (see, e.g. Shultz et al. 2019).

Because mCP stars usually show stable rotational modulation that is easily detectable from photometric data, they are usually searched via this channel (e.g. Hümmerich et al. 2016; Bernhard et al. 2021; Sikora et al. 2019a; Barron et al. 2020). However, close, non-eclipsing binary stars called ellipsoidal variables (ELLs; Beech 1985; Morris 1985) can show similar light curves with similar amplitudes and periods due to gravity darkening of their tidally deformed components, Doppler beaming, and the reflection effect (e.g. Faigler et al. 2012; Green et al. 2023). As discussed by Skarka et al. (2022), it is not possible to distinguish between a spotted rotationally variable star and an ELL star from single-channel photometry. Faigler et al. (2012) gave examples of seven ELL stars confirmed spectroscopically that show light curves perfectly mimicking rotational modulation seen in single spotted stars. Green et al. (2023) found that only about 50% of a suspected 97 ELL variables show clear radial-velocity variations that firmly confirm their variability, leaving ample space for misclassification. In addition, pulsations might mimic rotational variability, preventing the proper classification and interpretation of the photometric data (see the discussion in Skarka et al. 2022; Skarka & Henzl 2024).

Among O-F main-sequence stars, at least 50% of stars are variable (Gaia Collaboration 2019; Skarka et al. 2022; Skarka & Henzl 2024). The subject of this work was stars that show stable sinusoidal brightness variations, suggesting spots or ellipsoidal variability. Because it is impossible to distinguish spots from binarity based solely on the light-curve shape, our main goal was to find out which stars are bound in binary systems and identify candidates for spotted stars based on spectroscopy, particularly the radial-velocity analysis. From an initial sample of almost 46 000 objects in the TESS data (Ricker et al. 2015), we defined a sample of more than a hundred bright stars showing sinusoidal brightness variations with the selection procedure described in Section 2. For 35 stars, we complemented the TESS light curves with spectroscopic data from three high-resolution spectrographs (Section 3). We analysed each star individually, employing these spectroscopic observations, photometric information from TESS, and results from Gaia (Section 4). We discuss and conclude our results in Sections 5 and 6.

2. Sample definition

The sample of hot main-sequence stars used in this paper was based on the photometric observations from the TESS mission (Ricker et al. 2015). Data products include target pixel files (TPFs), light-curve files (LCFs), and full-frame images (FFIs) processed by the TESS Science Processing Operations Centre (SPOC; Jenkins et al. 2016). The analysis was carried out on LCFs with the provenance name TESS-SPOC, as most stars lacked data with the SPOC designation. Because the Quick-Look Pipeline (QLP) removes large-amplitude trends (Huang et al. 2020) and, in its first years, also removed stellar variability as noted by Skarka et al. (2022), we opted for a more conservative approach and have not used the QLP data. Similarly to Skarka et al. (2022), we applied no additional detrending, since the pre-search data conditioning simple aperture photometry (PDCSAP) fluxes were generally free of significant outliers and trends.

2.1. Initial sample

The initial sample of stars was constrained from the TESS input catalogue (TIC) v8.0 (Stassun et al. 2018) using two criteria. The first criterion restricted the sample to stars with variability associated with the radiative processes in their envelopes. Because there is no exact boundary between the hot stars with radiative envelopes and the cold stars with convective envelopes, we considered several lower limits of the effective temperatures ($T_{\rm eff}$): 6000 K as the minimum $T_{\rm eff}$ of F-type stars and 6700 K as the temperature that defines the transition between radiative and convective envelopes related to the Kraft break (Anders & Pedersen 2023; Brun & Miesch 2008). To account for stars near the transition region and minimise contamination from stars whose variability is associated with convective processes, we adopted a value of 6500 K. The second criterion limited the observed magnitude in the Johnson V band to stars brighter than $V = 9$ mag. It was chosen for practical reasons – we only selected stars that were suitable as targets for high-resolution echelle spectra taken with 1-metre class telescopes. More details about the instruments used can be found in Section 3.

The initial sample contained 45 780 stars. We collected available data from MAST using LIGHTKURVE software (Lightkurve Collaboration 2018; Barentsen & Lightkurve Collaboration 2020). For quick visual examination of the targets, we generated figures similar to those from Skarka et al. (2022) that contain key stellar characteristics. These images were generated in December 2023 using available data up to sector 72 (Cycle 6) of the TESS mission.

To analyse the periodicity of unevenly sampled data, we constructed Lomb-Scargle periodograms (Lomb 1976; Scargle 1982) in a low-frequency regime (0–5 c/d) and a high-frequency regime (5–100 c/d) and included them in the visual representation images. The significance of the signal was assessed using the false alarm probability (FAP), which evaluates the likelihood that the peak arises from noise. We chose a 1% FAP threshold. The light curves were phased with the dominant frequencies from both the low- and high-frequency regimes. The visual representation images also contained an image of the observed object as seen by the TESS cameras for examination of the stellar background and identification of blends.

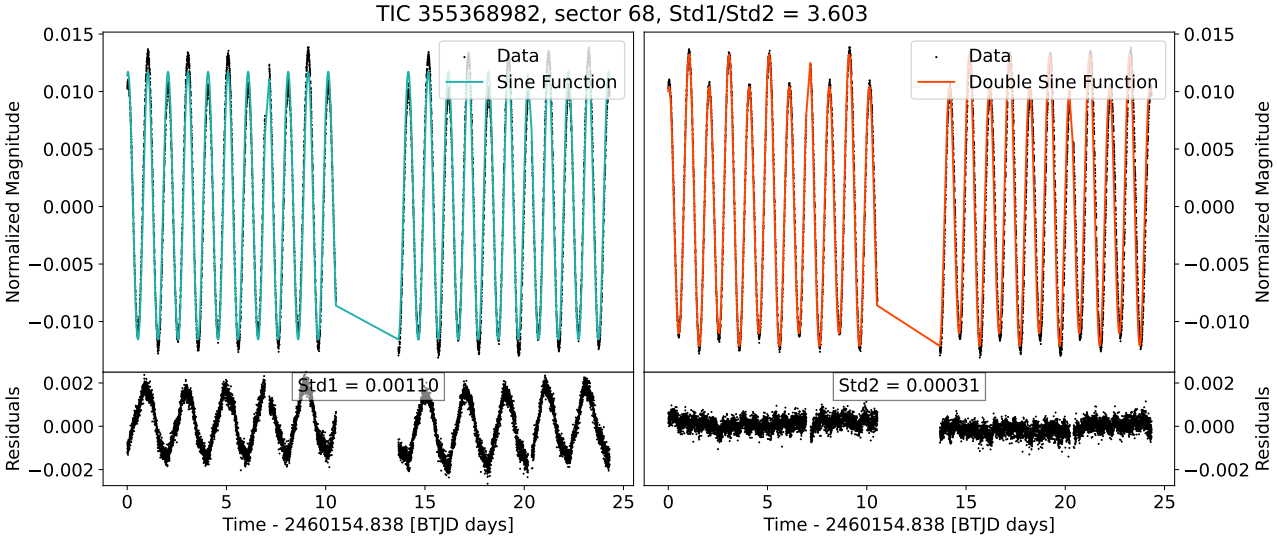

Fig. 1. Residuals after fitting data with single-sine (left panel) and two-sine (right panel) function. The figure contains standard deviations of residuals and their ratio used for identifying sinusoidal variability.

To obtain a more manageable dataset, we reduced the initial sample to objects that exhibited simple sinusoidal variations in the low-frequency regime, where various mechanisms can explain the variability. Variations in the high-frequency regime of hot stars are usually associated with pulsations, and their classification was beyond the scope of this work. Additionally, variations in the high-frequency regime could originate from Nyquist reflections. We employed a careful examination of the observed variability to identify and discard aliases during the candidate selection process, so the sample contained only low-frequency sinusoidal signals. We inspected the phased low-frequency light curves for shape deformations and minima of various depths that deviated from the simple sinusoidal shape, discarding objects that did not adhere to our requirements.

The reduced sample contained 472 objects. Nonetheless, visual inspection had its limitations and could not eliminate all non-sinusoidal light curves. These objects were carried forward with the understanding that a more thorough examination would be employed during finalisation of the sample in the next step.

2.2. Finalisation of sample

The presence of strictly sinusoidal variations was assessed by investigating the residuals after fitting a sinusoidal model to the photometric data. For each object from the reduced dataset, we selected one sector from the TESS observations least affected by instrumental deformations. The light curve was fitted with a simple sine function, y_{SSF} (Eq. (1)), and a function containing two sines, y_{TSF} (Eq. (2)), with frequencies f and $f/2$:

$$y_{\mathrm{SSF}} = a_1 \sin(2\pi f t + \phi_1), \tag{1}$$

$$y_{\mathrm{TSF}} = a_1 \sin(2\pi f t + \phi_1) + a_2 \sin(\pi f t + \phi_2). \tag{2}$$

An example of a figure used for the evaluation of light-curve shapes is shown in Fig. 1, where the blue and orange curves are model fits based on Eqs. (1) and (2), respectively. We calculated the difference between the data and individual models, which are shown in the residuals plots in Fig. 1, and evaluated the goodness of each fit by estimating their standard deviations (STDs).

Table 1. Distribution of stars rejected due to criteria imposed by the study of their residuals.

Criteria	N	Percentage (%)
Residuals ratio above 1.1	171	36.2
Light curve modulation	47	10.0
Shape or period change	14	3.0
Non-sinusoidal shape	132	27.9
Final sample	108	22.9

The fitted models were compared by calculating the ratio of STDs for the function with two sines and the single-sine function. We applied four criteria for the selection of sinusoidal variables from the reduced sample. First, the residual ratio needed to be below a value of 1.1. A ratio close to 1 indicated an ideal case where both functions fit the data in the same manner; however, due to data scatter, the two-sine function fit the data better in almost all cases. A ratio above 1.1 was empirically determined as the threshold where the two-sine function fitted the data significantly better, indicating that two consecutive minima had different depths that could not be explained by data scatter. These objects were rejected from the final sample, as these variations indicated their binary nature.

The second criterion rejected stars that exhibited light-curve modulation due to beating. The amplitude of variations periodically changes with time as the star pulsates. As stated before, the classification of pulsation modes is beyond the scope of this work, and these objects were rejected. The third criterion discarded stars that changed the shape of their light curves or the period of variations, while the fourth rejected objects with visible periodic trends in their residuals caused by a non-sinusoidal shape. The number of stars eliminated using each criterion and the targets contained in the final sample can be seen in Table 1.

The final sample of stars contained 108 objects that were divided into stars observed in the northern and southern hemispheres based on their declination angles. The distribution of spectral types in the final sample can be seen in Table 2.

Table 2. Distribution of spectral types in final sample of stars.

Type	$T_{\rm eff}$ (K)	Position	N	Percentage (%)
O	>25 000	north	0	0
		south	0	0
B	11 000–25 000	north	9	8.3
		south	18	16.7
A	7500–11 000	north	25	23.2
		south	31	28.7
F	6500–7500	north	11	10.2
		south	14	13.0

3. Spectroscopic observations

We supplemented the photometric data with spectroscopic observations that provided further insight into the origin of the photometric variability. From the 108 objects in the final sample, 45 targets were available for spectroscopic observations in the north with the Ondřejov Echelle Spectrograph (OES; Koubsky et al. 2004; Kabáth et al. 2020) and MUSICOS (Pribulla et al. 2024), while 63 targets were available for southern observations with PUCHEROS+ (Antonucci et al. 2025).

The Ondřejov Echelle Spectrograph is a high-resolution instrument mounted on the 2-metre Perek telescope at Ondřejov Observatory. It covers the 3870–9200 Å wavelength range with a spectral resolving power of R = 51 600, centred at 5000 Å (Koubsky et al. 2004). The long-term radial-velocity (RV) stability is approximately 200–300 ms^{-1} (Kabáth et al. 2020). An iodine absorption cell can be used as a wavelength reference for more precise RV measurements (Karjalainen et al. 2022). The limiting observation magnitude in the V filter is around 13 mag (Kabáth et al. 2020).

A high-dispersion echelle spectrograph MUSICOS is mounted at the 1.3-metre telescope located at Skalnaté Pleso Observatory (altitude of 1786 m above sea level). The high altitude reduces atmospheric turbulence and lowers water vapour content, improving the quality of spectroscopic observations. MUSICOS covers a spectral range from 4250–7375 Å, with a spectral resolution of R = 25 000-38 500, depending on the focusing (Pribulla et al. 2024). Pribulla et al. (2024) reported the RV stability of 100–200 m s^{-1}.

Another instrument that benefitted from its high-altitude location was PUCHEROS+ (Antonucci et al. 2025), located at the ESO La Silla observatory at 2400 m above sea level. Mounted on an ESO E152 1.52-metre telescope, PUCHEROS+ covers a spectral range from 4000–7300 Å, with R = 18 000 and an RV precision of 30 m s^{-1}. It was installed as a part of the PLATO spectroscopic follow-up programme and was replaced by the PLATOSpec instrument in November 2024 (Kabáth et al. 2025).

Observations lasted from May to September 2024 in the southern hemisphere and from April 2024 to July 2025 in the north. Observing all 108 targets was not feasible based on the available observation time, so we selected the best candidates for spectroscopic follow-up.

We used the Image Reduction and Analysis Facility (`IRAF`; Tody 1986) for the data reduction and RV estimations. We performed standard procedures of bias and flat-field corrections. For the removal of the cosmic hits, we used the `Dcr` routine (Pych 2004). The spectra were calibrated using Thorium-Argon lamps and corrected with the heliocentric RV and JD corrections. The RVs were determined relative to a template spectrum using the cross-correlation method implemented in the `Fxcor` task within `IRAF`. The resulting cross-correlation function (CCF) provided the RV shift between the two spectra caused by the Doppler effect. The reference spectrum was selected as the highest quality spectrum out of the observations. For targets with multiple visible components, the spectra were compared with a single-star template of a similar spectral type from Štegner (2020). All steps in the data reduction were performed with custom semi-automated `IRAF` scripts.

4. Analysis

We examined the sinusoidal variability of 35 objects with spectroscopic follow-up. Photometric data were first examined in December 2023 during the construction of the initial sample; however, since then, TESS has continued observations, providing new data for several targets. The extended time baseline was used for a more precise determination of the variability period. Frequency spectra were examined with a software package, `Period04` (Lenz & Breger 2004), to identify high-frequency signals, model the light curves, and refine frequencies, amplitudes, and phases.

Using the new TESS data, the difference between the initial variability period estimate and the period derived with `Period04` was less than one minute for 18 targets. However, for 17 objects, discrepancies reached up to 21 minutes, potentially blurring, shifting, or distorting the phase-folded light curves and RV curves. In the rest of the analysis, we used period estimates from `Period04`.

The majority of the targets did not exhibit high-frequency signals, suggesting the variability was dominated by a single periodic component. Ten objects contained high-frequency signals with significantly lower amplitudes (around 18 times lower on average). In several cases, the secondary peaks were identified as harmonics (integer multiples of the dominant frequency) or known instrumental artefacts. For two objects – TIC 16878120 and TIC 88815918 – the secondary peaks were within the Rayleigh resolution limit of the dominant frequency, meaning the dominant signal was not fully removed during prewhitening. This signal could be explained by secular variations of the period caused by a variety of mechanisms, including the evolution processes of pulsators and dynamic interactions in binaries. TIC 320692159, on the other hand, displayed high-frequency peaks typical of δ-Scuti pulsators (DCST; see, e.g. Breger & Stockenhuber 1983; Breger 2000; Skarka et al. 2022).

The classification criteria were based on the combination of light curves (LCs; see, e.g. the top plot of Fig. 2) obtained from photometric data and RV curves from spectra (see, for example, the bottom plot of Fig. 2). We examined LCs and RVs phase-folded with the dominant period, P, and twice the dominant period, $2P$ (see, e.g. the first and the second columns of Fig. 4, respectively). The spectral features (such as hydrogen lines), and CCFs (see Fig. 3) were used to support the classification. In cases with low signal-to-noise ratio (S/N), where the RV fit failed to converge, they also provided evidence based on identifiable features. The detailed description of the classification of individual variability types is provided in the following sections. Each object was cross-referenced with the Simbad database (Wenger et al. 2000), VSX catalogue (Watson 2006), and catalogue of

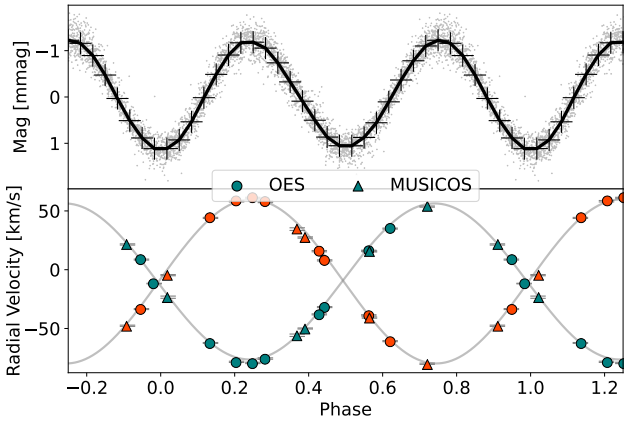

Fig. 2. Example of LC (top plot) showing original (grey dots) and binned data (black crosses) and RV curve (bottom plot) for a spectroscopic binary with two visible components – TIC 257456854.

chemically peculiar stars (Renson & Manfroid 2009). We found 15 objects to be known as variable sources in Simbad; 12 objects were known as variable stars and present in the VSX, while seven stars were marked as chemically peculiar in Renson & Manfroid (2009). We note that detailed investigation of these objects, their chemical abundances, and modelling of the binary systems is beyond the scope of the current study.

4.1. Binary stars

Objects in the sample had low amplitudes and short periods, which, in the case of binary stars, can be explained by ellipsoidal variability. At least one of the components has a gravitationally distorted shape that causes brightness variations with two similar minima depths per cycle. The true photometric period is twice the observed one; therefore, it is necessary to examine $2P$ phase-folded data. The non-sinusoidal shape of the RV curve can be attributed to systems with eccentric orbits, Doppler beaming (change in observed flux due to the motion of a component towards or away from the observer), star spots, or a reflection effect (the mutual irradiation of the components). Binary stars were distinguished from the sample in several ways, each of which can be explained by the orbital motion of the components around a common centre of mass.

First, the spectral lines of both components were visible, leading to two separate RVs in anti-phase, as seen in the bottom plot of Fig. 2. The true orbital period of these components was $2P$, and the LCs and RVs remained correlated, with no RV shift (with respect to the template) during the minimum brightness; at that point, the semi-major axis of the binary system was aligned with the observer's line of sight. Moreover, we observed no Doppler shift. The multiplicity of the signal could be verified by the CCFs, as seen in Fig. 3. These objects were marked as double-lined spectroscopic binaries (SB2).

In the second case, we observed only one component of the binary system, which was marked as a single-line spectroscopic binary (SB1; see Fig. 4). When the data were phase-folded with period, P, we observed weak or no variations in RVs. However, when folded with $2P$, the RV curve revealed a clear monotonic variation (see the bottom plots of Fig. 4). Additionally, the bottom left plot in Fig. 4 mimics the variations caused by SB2, even though the measured spectra had only one visible component. This effect can be explained by phase folding an RV curve

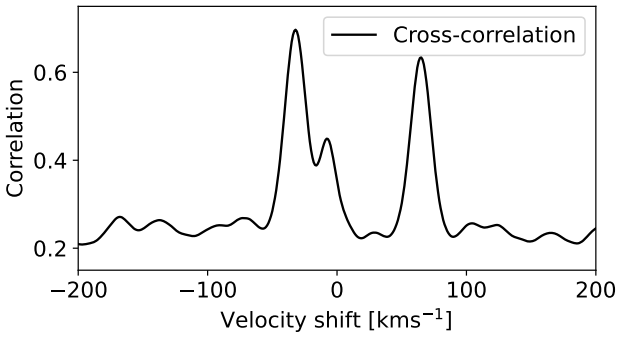

Fig. 3. CCF of TIC 14400891. This object is a candidate for a triple-star system, based on the number of correlation peaks.

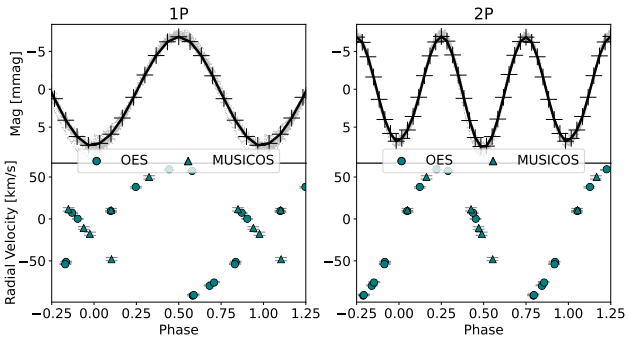

Fig. 4. Comparison of LC (top plots) showing original (grey dots) and binned data (black crosses) and RVs (bottom plots) for a spectroscopic binary with one visible component phased with 1P (first column) and 2P (second column) – TIC 21673730.

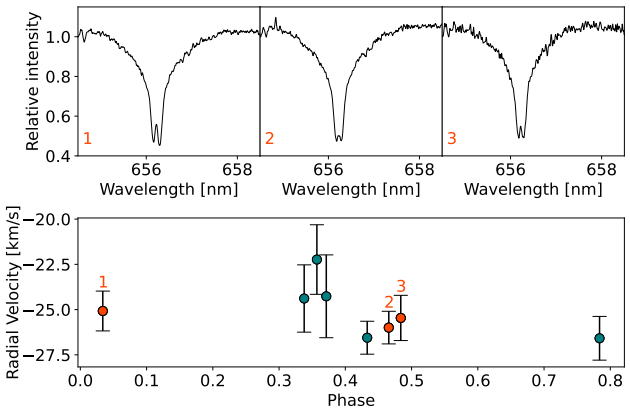

Fig. 5. RV curve of TIC 174214184 measured with OES, where points highlighted in red show corresponding spectra, with a zoomed-in view of the Hα that shows lines of both components.

with half the correct period and should not be confused with variations caused by SB2.

Lastly, in cases where the extraction of correct RVs was not possible due to unresolved but apparent components, the multiplicity could be revealed from the spectra. Fig. 5 shows an example of an object where RVs showed no variability, but spectral lines of both components were visible.

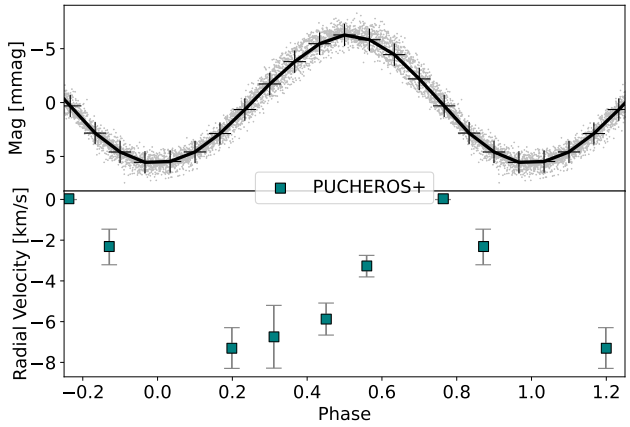

Fig. 6. Example of LC (top) showing original (grey dots) and binned data (black crosses) and RV curve (bottom) for a pulsating star – TIC 205913291.

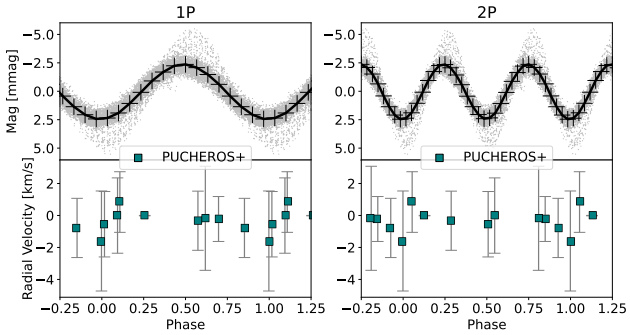

Fig. 7. Example of LC (top panels) showing original (grey dots) and binned data (black crosses) and RV curve (bottom panels) for a candidate for spots with RVs close to zero – TIC 61449214.

4.2. Pulsating stars

When a star pulsates, its outer layers periodically expand and contract in response to its pulsation mode, leading to a change in effective temperature. During compression, the material heats up and the effective temperature rises, increasing the brightness. During expansion, it cools and its brightness decreases. This process introduces a phase difference of $\pi/4$ between the LC and RV curve. In the sample of targets, pulsating variables, denoted Pu, were found by examining the phase shift of LC and RVs phased with P. These objects exhibited zero RV at maximum and minimum brightness, with peak (or trough) RV occurring midway between the flux extrema. An example of such a case from the sample can be seen in Fig. 6.

4.3. Candidates for spots

Photometric spots in the atmospheres of hot stars redistribute radiation and lead to different LC shapes in different photometric filters, with variations of the order of millimagnitudes. Since the spots are confined to the rotating atmosphere, they do not induce a significant RV shift in the observed light. The RV variations caused by spots have very low amplitudes. Spotted stars were identified based on the appearance of their RVs, supported by slight deformations of LCs. RV measurements were close to zero (see Fig. 7), with only slight variations in several cases (see Fig. 8).

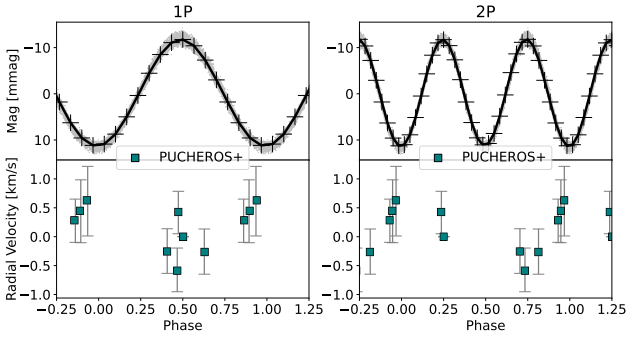

Fig. 8. Example of LC (top panels) showing original (grey dots) and binned data (black crosses) and RV curve (bottom panels) for a candidate for spots with RVs close to zero – TIC 113150902.

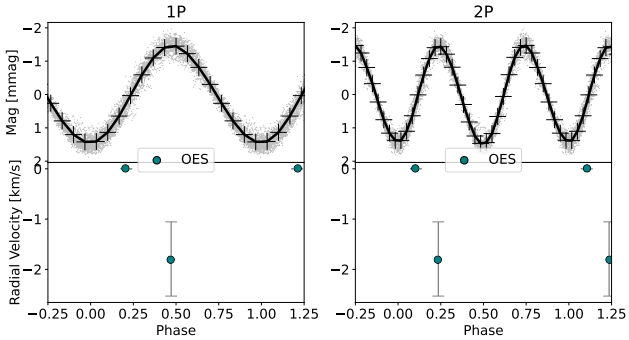

Fig. 9. Example of LC (top panels) showing original (grey dots) and binned data (black crosses) and RV curve (bottom panels) for a star with uncertain classification with too few RV data points – TIC 88815918.

Another way to produce photometric variability of the order of millimagnitudes with RVs close to zero is by observing a binary system with low inclination angles, nearly perpendicular to the orbital plane. These two cases cannot be distinguished with LCs and RVs alone, so they are marked as both 'spots' and 'binary'. Their classification remains a matter for future work.

4.4. Uncertain classification

Even with the combination of photometric and spectroscopic data, the classification for some targets was unclear. These objects were attributed the "uncertain" tag for several reasons. First, the classification was not possible for objects with too few spectroscopic measurements (see Fig. 9). Similarly, the origin of the variations was unclear if the RVs showed variability when phased with both P and $2P$. Fig. 10 shows an example of such an object, where measurements in a specific phase could help determine the variability mechanism. Additionally, for some objects, the RV curve showed no periodic variations, but the scatter of the data was significant and could not be attributed to the noise (see Fig. 11). Lastly, the object was assigned an unclear classification if additional processing revealed it was a blend, and the variable signal originated from a nearby source.

5. Discussion

Based on the classification criteria outlined in Sect. 4, we identified 18 binary stars, one pulsating star, nine spotted-star candidates, and seven objects with uncertain classification (see Table A.1). We conducted a detailed examination of sky

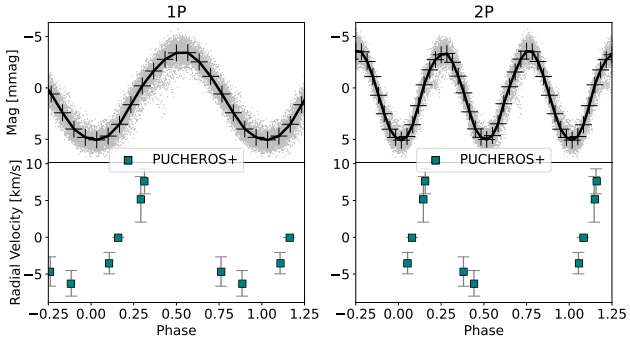

Fig. 10. Example of LC (top panels) showing original (grey dots) and binned data (black crosses) and RV curve (bottom panels) for a star with uncertain classification, where we were unable to determine the variability mechanism due to the variability in both 1P and 2P – TIC 292207311.

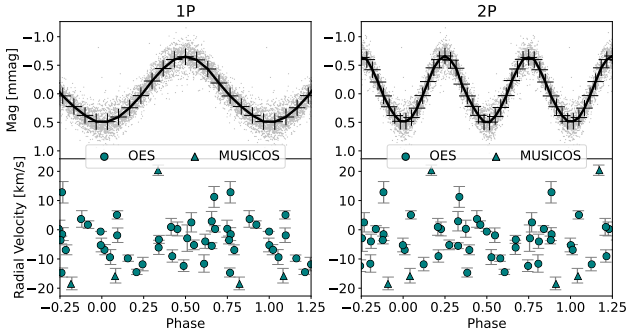

Fig. 11. Example of LC (top panels) showing original (grey dots) and binned data (black crosses) and RV curve (bottom plots) for a star with uncertain classification and a large scatter of the data – TIC 16878120.

background for each object using the built-in functions in the LIGHTKURVE library, TPF PLOTTER (Aller et al. 2020), and TESS LOCALIZE (Higgins & Bell 2022). We searched for possible sources of contamination up to 6 mag fainter than the target and calculated the origin of the variable signal using the data in individual pixels of TPFs. The origin of the variability was then associated with an object in the field of view (FoV). The vast majority of targets were identified as the origin of the variable signal, with only a single target identified as a blend (TIC 444577764).

The final sample included 18 objects identified as binary systems. For eight systems, we confirmed the previous classification from Simbad (see Table A.1). In previous publications, TIC 220485766 was identified as either a pulsating or binary star (Gaia Collaboration 2022b,a); VSX lists this object as a pulsating star. Based on the spectroscopic data, we support the binary interpretation. TIC 21673730 was previously identified as a pulsator (Smalley et al. 2011; Watson 2006). However, this classification was based only on photometric data from the SuperWASP survey of Am pulsators. Spectroscopic observations of this object revealed variability that can only be attributed to a binary system. The remaining eight stars were newly identified SB1 or SB2 binary stars with no previous classification. Since the SB1/SB2 distinction depends on the quality of the observations, we assigned these labels based solely on the available data and did not place significant emphasis on this division. Four of the sample stars identified as SB1 or SB2 were marked as metallic stars by Renson & Manfroid (2009), which is not surprising because about 70% of metallic stars are found in binary systems (Abt 1961; Abt & Levy 1985; Carquillat & Prieur 2007). This chemical peculiarity might also contribute to light variations.

For all binary stars in the final sample, the observed variability might result from a combination of rotational modulation, reflection, Doppler beaming, and tidal interaction between the components. This complicates the retrieval of orbital parameters and makes detailed modelling beyond the scope of this work.

Based on the classification criteria, we identified only one pulsating object in the final sample. TIC 205913291 was marked in VSX (Watson 2006) as a variable star with unspecified variability type and was identified in the K2 observing campaign (Armstrong et al. 2016). This star is marked as a magnetic CP star of Bp8 Si spectral type in Renson & Manfroid (2009). However, the amplitude of about 10 kms^{-1} suggests that the RV variations are more likely caused by pulsations than by chemical spots.

Out of 35 objects with the spectroscopic follow-up, we identified nine candidates for spotted stars. All except one (TIC 184607315) are located in the southern hemisphere and each has an effective temperature above 7000 K, which is consistent with the formation theory of stable photometric spots via diffusion and settling of different chemical elements (Michaud 1970; Michaud et al. 1976).

TIC 66497441 and TIC 184607315 exhibited long-term trends that could be attributed to a long-period orbital motion of a binary system around a common centre with a third body. After removing the long-term trend, the corrected RVs were inconclusive, and the stars were classified as spots/binary+SB because we could not distinguish between rotational modulation due to spots and proximity effects in binary systems with low inclination. Confirming the presence of photometric spots on the surface of these stars would require detailed analysis of spectra, chemical abundances, and multi-colour photometry, which lies outside the scope of this work.

Uncertain objects comprise 20% of the sample (see Table A.1). TIC 444577764 was identified as a blend during the background analysis mentioned above. This object was a part of a very crowded field, with a bright star blending into the aperture. VSX knows this object as a rotationally variable star (Watson 2006). TIC 88815918 had only two spectroscopic observations with a good S/N and many spectral lines. The object lacked the presence of a second companion in the spectral lines, even though the spectra were taken during quadrature. It is very likely that the object is not an SB2; however, the lack of additional data makes further classification impossible.

Similarly, TIC 310932102 shows RV variability when phased with $1P$. However, due to the scatter of the data, the lack of additional information makes the classification unclear. TIC 292207311 and TIC 448876509, known as variable stars in VSX (Watson 2006), showed variability when phased with both P and $2P$, but they lacked phase coverage between 0.5 and 1.0, which made the determination of variation mechanism impossible. TIC 16878120 and TIC 218160121 both exhibited a large scatter of the data (the standard deviation was 8.2 kms^{-1} and 6.0 kms^{-1}, respectively) that could not be attributed to noise. TIC 16878120 additionally exhibited a long-term trend that could not be removed due to poor data coverage. This trend could be explained by instrumental effects or changes in observing conditions; however, given the consistency of the RVs obtained from OES and MUSICOS under different conditions and instrumental setups, we are confident of the reliability of the measurements. The observed scatter in RVs could be attributed to intrinsic long-term variability. However, the dataset does not provide sufficient coverage to support this hypothesis, making the fitting and correction of RVs impossible. In the case of TIC 218160121, the

scatter in RVs might be due to chemical peculiarity (Renson & Manfroid 2009).

6. Conclusions

We identified a sample of 108 F- to O-type main-sequence stars with sinusoidal brightness variations on the level of millimagnitudes that can be explained by different variability mechanisms – such as binarity, pulsations, or rotational variability due to photometric spots. This work highlights the complexity of stellar classification and the need for a detailed, individual approach.

We employed a careful, multi-step selection process involving automated scripts and manual inspection to select only stars with clean monotonic sinusoidal variations. These stars were spectroscopically observed by using three spectrographs: OES and MUSICOS in the northern hemisphere and PUCHEROS+ in the southern hemisphere. We obtained spectra for 35 objects in the sample and used custom IRAF scripts to extract RVs of these targets. The sky background of each object was carefully analysed with Python routines, and the contamination from nearby stars was considered.

The analysed targets were divided into four categories based on the appearance of their phase-folded LCs with respect to phase-folded RVs: binary systems, pulsating stars, spotted-star candidates, and objects with uncertain classifications (Table A.1). These categories reflect the characteristics of the chosen dataset, that is, mainly the small amplitude of photometric variations and variability linked to processes in the radiative envelopes of hot stars. Binary stars comprised more than 50 % of the analysed targets. This is not surprising, as the multiplicity fraction, depending on stellar environment, increases with stellar mass (Chini et al. 2012). Duchêne & Kraus (2013) reported the multiplicity fraction of 70 ± 9% for O-type stars, 45 ± 5% for B-type stars, and 30–40 % for stars between spectral types B5 and F.

Candidates for spotted stars represent one fourth of our sample stars. However, this number could change with the proper identification of rotational variability through the detailed analysis of chemical abundances and multi-colour photometry. In literature, chemically peculiar stars with stable photometric spots in radiative atmospheres make up about 10 % of B to F-type stars (Hümmerich et al. 2018). We spotted only one pulsating star in our sample. The rest of the sample (about 20 %) was assigned an uncertain classification. With additional spectroscopic measurements, the variation mechanism of some of these objects could be resolved.

Our study revealed that in a random selection of stars with sinusoidal photometric variations, about half of them are binary stars. It is worth noting that we did not find any overlap between our sample and catalogues of chemically peculiar stars from LAMOST (Ghazaryan et al. 2018; Qin et al. 2019), and there was no overlap with magnetic stars (Rustem et al. 2023). Eight stars were found in the catalogue by Renson & Manfroid (2009). TIC 205913291 and TIC 226037840 are labelled as Bp9 Si and Bp8 Si, respectively, which points towards the magnetic chemically peculiar nature of these stars.

Nineteen stars from our sample have a remark about their variability in the literature. However, our classification is at least partially in agreement with literature in only nine of these stars. We revealed eight new binary systems, one new pulsating star, and nine candidates for spotted stars. However, these spot candidates might include binary systems with low inclination angles. These results highlight the discrepancies in catalogue values and the necessity of careful analysis and follow-up spectroscopic measurements, especially for objects where photometric data alone are insufficient for determining the variability mechanism.

Acknowledgements. We would like to thank the observers for their work. We acknowledge a bilateral mobility project between Slovak Academy of Sciences and Czech Academy of Sciences SAV-25-10. MV and TP acknowledge support from the Slovak Research and Development Agency â contract No. APVV-20-0148, and the VEGA grant of the Slovak Academy of Sciences No. 2/0031/22. MS acknowledges the support by Inter-transfer grant no LTT-20015. This paper includes data collected with the TESS mission and with the Perek telescope at the Astronomical Institute of the Czech Academy of Sciences in Ondřejov. Funding for the TESS mission is provided by the NASA Explorer Program. The TESS data were obtained from the MAST data archive at the Space Telescope Science Institute (STScI). This research made use of NASAâs Astrophysics Data System Bibliographic Services, and of the SIMBAD database, operated at CDS, Strasbourg, France.

References

Abt, H. A. 1961, ApJS, 6, 37
Abt, H. A., & Levy, S. G. 1985, ApJS, 59, 229
Abt, H. A., & Morrell, N. I. 1995, ApJS, 99, 135
Aerts, C. 2021, Rev. Mod. Phys., 93, 015001
Aerts, C., & Tkachenko, A. 2024, A&A, 692, R1
Aerts, C., Mathis, S., & Rogers, T. M. 2019, ARA&A, 57, 35
Alecian, G. 2015, MNRAS, 454, 3143
Aller, A., Lillo-Box, J., Jones, D., Miranda, L. F., & Barceló Forteza, S. 2020, A&A, 635, A128
Anders, E. H., & Pedersen, M. G. 2023, Galaxies, 11, 56
Antoci, V., Cantiello, M., Khalack, V., et al. 2025, A&A, 696, A111
Antonucci, L., Vanzi, L., Zapata, A. A., et al. 2025, MNRAS, 542, 1730
Armstrong, D. J., Kirk, J., Lam, K. W. F., et al. 2016, MNRAS, 456, 2260
Babcock, H. W. 1960, ApJ, 132, 521
Bagnulo, S. 2003, in IAU Symposium, Vol. 210, Modelling of Stellar Atmospheres, eds. N. Piskunov, W. W. Weiss, & D. F. Gray, 209
Barentsen, G., & Lightkurve Collaboration. 2020, in American Astronomical Society Meeting Abstracts, 235, 409.04
Barron, J., Wade, G. A., Bowman, D. M., et al. 2020, in Stellar Magnetism: A Workshop in Honour of the Career and Contributions of John D. Landstreet, 11, eds. G. Wade, E. Alecian, D. Bohlender, & A. Sigut, 226
Beech, M. 1985, Ap&SS, 117, 69
Bernhard, K., Hümmerich, S., Paunzen, E., & Supíková, J. 2021, MNRAS, 506, 4561
Braithwaite, J., & Spruit, H. C. 2004, Nature, 431, 819
Breger, M. 2000, in Astronomical Society of the Pacific Conference Series, 210, Delta Scuti and Related Stars, eds. M. Breger & M. Montgomery, 3
Breger, M., & Stockenhuber, H. 1983, Hvar Observ. Bull., 7, 283
Brun, A. S., & Miesch, M. S. 2008, Stellar Convect. Simul. Scholarpedia, 3, 4278
Carquillat, J. M., & Prieur, J. L. 2007, MNRAS, 380, 1064
Chini, R., Hoffmeister, V. H., Nasseri, A., Stahl, O., & Zinnecker, H. 2012, MNRAS, 424, 1925
Donati, J. F., & Landstreet, J. D. 2009, ARA&A, 47, 333
Duchêne, G., & Kraus, A. 2013, ARA&A, 51, 269
Eldridge, J. J., & Stanway, E. R. 2022, ARA&A, 60, 455
Eyer, L., & Mowlavi, N. 2008, in Journal of Physics Conference Series, 118, Journal of Physics Conference Series (IOP), 012010
Eyer, L., Guy, L., Distefano, E., et al. 2018, Gaia DR2 documentation, Chapter 7: Variability, Gaia DR2 documentation, European Space Agency; Gaia Data Processing and Analysis Consortium. Online at `https://gea.esac.esa.int/archive/documentation/GDR2/`, 7
Faigler, S., Mazeh, T., Quinn, S. N., Latham, D. W., & Tal-Or, L. 2012, ApJ, 746, 185
Ferrario, L. 2018, Contrib. Astron. Observ. Skalnate Pleso, 48, 15
Fetherolf, T., Pepper, J., Simpson, E., et al. 2023, ApJS, 268, 4
Gaia Collaboration (Eyer, L. et al.) 2019, A&A, 623, A110
Gaia Collaboration 2022a, VizieR Online Data Catalog: Gaia DR3 Part 1. Main source (Gaia Collaboration, 2022), VizieR On-line Data Catalog: I/355. Originally published in: doi:10.1051/0004-63
Gaia Collaboration 2022b, VizieR Online Data Catalog: Gaia DR3 Part 3. Non-single stars (Gaia Collaboration, 2022), VizieR On-line Data Catalog: I/357. Originally published in: 2023A&A...674A...1G
Ghazaryan, S., Alecian, G., & Hakobyan, A. A. 2018, MNRAS, 480, 2953
Green, M. J., Maoz, D., Mazeh, T., et al. 2023, MNRAS, 522, 29
Henriksen, A. I., Antoci, V., Saio, H., et al. 2023, MNRAS, 520, 216

Higgins, M. E., & Bell, K. J. 2022, TESS-Localize: Localize variable star signatures in TESS Photometry, Astrophysics Source Code Library [record ascl:2204.005]
Huang, C. X., Vanderburg, A., Pál, A., et al. 2020, RNAAS, 4, 204
Hümmerich, S., Paunzen, E., & Bernhard, K. 2016, AJ, 152, 104
Hümmerich, S., Mikulášek, Z., Paunzen, E., et al. 2018, A&A, 619, A98
Jenkins, J. M., Twicken, J. D., McCauliff, S., et al. 2016, SPIE Conf. Ser., 9913, 99133E
Kabáth, P., Skarka, M., Sabotta, S., et al. 2020, PASP, 132, 035002
Kabáth, P., Skarka, M., Hatzes, A., et al. 2025, MNRAS, 545, staf1972
Karjalainen, M., Karjalainen, R., Hatzes, A. P., et al. 2022, A&A, 668, A26
Koubsky, P., Mayer, P., Čáp, J., et al. 2004, Publ. Astron. Inst. Czech. Acad. Sci., 92, 37
Kraft, R. P. 1967, ApJ, 150, 551
Kurtz, D. 2022, in Annual Conference and General Assembly of the, 1
Lenz, P., & Breger, M. 2004, in IAU Symposium, 224, The A-Star Puzzle, eds. J. Zverko, J. Ziznovsky, S. J. Adelman, & W. W. Weiss, 786
Lightkurve Collaboration (Cardoso, J. V. d. M., et al.) 2018, Astrophysics Source Code Library [record ascl:1812.013]
Lomb, N. R. 1976, Ap&SS, 39, 447
Lu, Z., Kong, X., Zhang, Y., Yi, Z., & Liu, M. 2025, AJ, 169, 270
Marchant, P., & Bodensteiner, J. 2024, ARA&A, 62, 21
Mathys, G. 2004, in IAU Symposium, 215, Stellar Rotation, eds. A. Maeder, & P. Eenens, 270
Maury, A. C., & Pickering, E. C. 1897, Ann. Harvard Coll. Observ., 28, 1
Michaud, G. 1970, ApJ, 160, 641
Michaud, G., Charland, Y., Vauclair, S., & Vauclair, G. 1976, ApJ, 210, 447
Morris, S. L. 1985, ApJ, 295, 143
Oksala, M. E., Wade, G. A., Townsend, R. H. D., et al. 2012, MNRAS, 419, 959
Petrosky, E., Hwang, H.-C., Zakamska, N. L., Chandra, V., & Hill, M. J. 2021, MNRAS, 503, 3975
Preston, G. W. 1974, ARA&A, 12, 257
Pribulla, T., Vaňko, M., Komžík, R., & Sivanič, P. 2024, Contrib. Astron. Observ. Skalnate Pleso, 54, 43
Pych, W. 2004, PASP, 116, 148
Qin, L., Luo, A. L., Hou, W., et al. 2019, ApJS, 242, 13
Qin, L., Luo, A. L., Hou, W., et al. 2021, AJ, 162, 32
Renson, P., & Manfroid, J. 2009, A&A, 498, 961
Ricker, G. R., Winn, J. N., Vanderspek, R., et al. 2015, J. Astron. Telesc. Instrum. Syst., 1, 014003
Royer, F., Zorec, J., & Gómez, A. E. 2007, A&A, 463, 671
Rustem, A., Lü, G.-L., Liu, J.-Z., et al. 2023, Res. Astron. Astrophys., 23, 095024
Samus, N. N., Kazarovets, E. V., Durlevich, O. V., Kireeva, N. N., & Pastukhova, E. N. 2017, Astron. Rep., 61, 80
Scargle, J. D. 1982, ApJ, 263, 835
Schneider, F. R. N., Ohlmann, S. T., Podsiadlowski, P., et al. 2019, Nature, 574, 211
Schnell, A. 2008, Contrib. Astron. Observ. Skalnate Pleso, 38, 87
Shultz, M., Rivinius, T., Wade, G. A., et al. 2018, MNRAS, 475, 839
Shultz, M. E., Wade, G. A., Rivinius, T., et al. 2019, MNRAS, 490, 274
Sikora, J., David-Uraz, A., Chowdhury, S., et al. 2019a, MNRAS, 487, 4695
Sikora, J., Wade, G. A., Power, J., & Neiner, C. 2019b, MNRAS, 483, 2300
Skarka, M., & Henzl, Z. 2024, A&A, 688, A25
Skarka, M., Žák, J., Fedurco, M., et al. 2022, A&A, 666, A142
Smalley, B., Kurtz, D. W., Smith, A. M. S., et al. 2011, A&A, 535, A3
Stassun, K. G., Oelkers, R. J., Pepper, J., et al. 2018, AJ, 156, 102
Štegner, D. 2020, Spectroscopic templates for the Ondrejov Echelle Spectrograph [accessed 19 October 2025]
Tody, D. 1986, SPIE Conf. Ser., 627, 733
Townley, S. D. 1913, PASP, 25, 239
Watson, C. L. 2006, J. Am. Assoc. Var. Star Observers, 35, 318
Wenger, M., Ochsenbein, F., Egret, D., et al. 2000, A&AS, 143, 9
Zinnecker, H., & Yorke, H. W. 2007, ARA&A, 45, 481

Appendix A: Classification table

Table A.1. Classification of our sample of stars. The column 'Type' gives classification in this work, column 'CP' gives the spectral type from Renson & Manfroid (2009), column 'VSX' gives the classification in Watson (2006). The other columns are self-explanatory.

TIC	RA (deg)	DEC (deg)	f (c/d)	P (d)	$T_{\rm eff}$ (K)	Type	CP	VSX type
5638336	32.327	28.394	0.469	2.132	9212	SB1	...	...
12321432	32.835	64.146	0.370	2.703	13491	SB2	...	...
14400891	127.769	54.081	0.435	2.299	6790	SB2	...	...
16878120	232.692	34.466	3.187	0.314	9677	uncertain	...	...
21673730	255.722	31.690	0.623	1.605	7879	SB1	A2-	GDOR
31623275	289.076	-34.446	1.250	0.800	10850	SB1	...	ACV|roAm|roAp|SXARI
61449214	228.484	-26.051	1.549	0.646	7697	spots/binary	...	...
66497441	356.050	-18.277	2.612	0.383	11505	spots/binary+SB	...	...
84756974	249.991	-39.789	3.567	0.280	9265	spots/binary	...	...
88815918	27.046	16.956	0.836	1.196	10471	uncertain	...	...
113150902	277.024	-38.357	0.990	1.010	11200	spots/binary	...	VAR
135081803	184.888	-40.839	0.750	1.333	7861	SB2	...	...
137800207	344.066	-23.849	1.661	0.602	7023	spots/binary	...	...
160644410	223.727	-36.430	0.671	1.490	9425	spots/binary	...	...
174214184	234.737	-41.098	0.937	1.067	6914	SB2	A1-F2	...
184607315	31.603	38.900	0.814	1.229	9390	spots/binary+SB	...	...
205913291	250.398	-28.586	0.783	1.277	10853	Pu	B9 Si	VAR
212031970	248.419	-31.289	1.887	0.530	9688	SB2	...	VAR
218160121	261.994	-44.721	4.568	0.219	7514	uncertain	A1-	...
220485766	343.501	-54.727	1.254	0.797	8715	SB1	...	DSCT|GDOR|SXPHE
226037840	247.367	-46.261	2.013	0.497	10393	spots/binary	B8 Si	MISC
257456854	257.821	24.252	0.886	1.129	6750	SB2	...	...
279821618	239.879	-40.865	2.181	0.459	8574	spots/binary	...	...
292207311	230.933	-27.952	1.264	0.791	7317	uncertain	...	...
293069615	254.137	-66.109	0.795	1.258	8609	SB2	...	...
302581695	133.482	35.538	0.986	1.014	9101	SB1	...	ELL
302666414	163.005	55.355	0.623	1.605	7419	SB1	A8-F3	...
310932102	262.096	29.838	0.767	1.304	9955	uncertain	...	...
320692159	271.163	27.115	1.583	0.632	7646	SB2	...	VAR
342829903	205.359	-67.882	0.633	1.580	6666	SB2	...	...
347699402	263.048	21.264	0.304	3.289	8520	SB1	...	...
351532879	309.160	-63.121	0.486	2.058	6658	SB2	...	...
419610625	320.367	-66.667	0.718	1.393	7832	SB1	A3-F0	...
444577764	267.783	-35.337	1.612	0.620	11608	uncertain	...	ACV|roAm|roAp|SXARI
448876509	214.291	-68.407	0.347	2.882	11798	uncertain	...	VAR

Appendix B: Measured relative radial velocities

Table B.1. Relative radial velocities for targets in our sample of stars

HJD	RV (km s^{-1})	err (km s^{-1})	HJD	RV (km s^{-1})	err (km s^{-1})	HJD	RV (km s^{-1})	err (km s^{-1})
TIC 5638336 (OES)			TIC 16878120 (OES)			TIC 84756974 (PUCHEROS+)		
2460559.5210	0.00	0.00	2460774.4907	0.31	1.10	2460528.6413	-0.59	6.00
2460576.6100	-0.87	0.43	2460776.5042	5.10	1.40	2460544.5228	-3.29	11.00
2460663.3410	18.59	0.22	2460794.5276	2.55	3.30	2460545.6120	3.85	7.90
2460672.3449	34.48	0.31	2460795.5069	2.93	3.30	2460559.5409	-5.36	5.50
2460673.3094	41.16	0.30	2460796.4835	-1.49	2.20	2460567.5269	-5.14	8.60
2460674.3121	11.54	0.46	2460797.4726	1.76	1.30	TIC 88815918 (OES)		
TIC 12321432 (OES)			2460805.5475	-5.45	1.00	2460559.5065	0.00	0.00
2460559.5636	-6.53	3.50	2460809.4505	-1.87	2.50	2460576.5639	-1.79	0.74
2460672.3793	74.86	5.30	2460826.4716	-3.29	1.40	TIC 113150902 (PUCHEROS+)		
2460673.3545	-9.25	2.70	2460828.4851	-3.50	1.30	2460495.8025	0.00	0.00
2460674.3597	73.56	5.50	2460836.4545	-9.72	1.10	2460499.8156	0.42	0.37
2460683.3540	67.54	6.40	2460840.4902	-6.82	1.70	2460500.7593	-0.25	0.39
TIC 14400891 (OES)			2460844.3815	-8.98	2.10	2460535.5768	0.28	0.37
2460428.3782	-80.88	0.61	2460846.3796	-6.86	1.70	2460543.7352	0.61	0.60
2460428.3782	93.27	0.64	2460847.3862	-5.21	2.40	2460545.7148	0.44	0.54
2460428.3782	44.18	1.60	2460850.4046	-3.94	2.40	2460555.5517	-0.26	0.39
2460429.4306	-14.65	0.58	2460855.3846	-12.29	2.00	2460573.5788	-0.57	0.38
2460429.4306	32.13	0.48	2460856.3453	-5.17	1.70	TIC 135081803 (PUCHEROS+)		
2460430.3853	-72.07	0.55	TIC 16878120 (MUSICOS)			2460516.4642	-106.71	2.00
2460430.3853	82.25	0.43	2460712.5716	20.39	1.80	2460516.4642	72.70	2.70
2460430.3853	41.29	1.30	2460859.3360	-15.73	2.50	2460518.5051	-87.05	2.00
2460431.3718	-52.44	0.69	2460879.3352	-18.37	2.20	2460518.5051	54.79	2.90
2460431.3718	63.30	0.58	TIC 21673730 (OES)			TIC 137800207 (PUCHEROS+)		
2460431.3718	38.73	1.50	2460428.4812	56.57	0.68	2460494.9256	2.80	3.50
2460433.3597	-69.98	0.44	2460430.4977	-51.01	0.56	2460495.8530	4.13	5.20
2460433.3597	87.81	0.52	2460431.4725	58.49	0.40	2460499.9003	6.07	2.40
2460433.3597	32.85	1.30	2460433.4597	-79.26	0.59	2460500.9409	5.12	2.70
2460435.3190	-80.25	0.57	2460435.4204	0.05	0.04	2460510.7198	3.46	2.70
2460435.3190	95.05	0.45	2460511.3746	37.66	0.87	2460518.6863	2.74	3.20
2460435.3190	30.78	1.40	2460512.3762	7.19	0.74	2460544.6784	-0.24	3.70
2460436.3255	-9.37	0.77	2460520.3333	-53.80	0.51	2460545.7895	-0.92	3.80
2460436.3255	28.02	0.41	2460523.3454	-75.34	0.63	2460559.8369	3.02	3.90
2460709.4034	-57.62	0.51	2460526.3528	-90.85	0.78	2460565.7616	0.76	4.10
2460709.4034	71.92	0.64	2460526.3617	-90.13	0.60	2460568.7572	0.00	0.04
2460709.4034	25.81	1.10	2460559.2686	9.19	0.76	TIC 160644410 (PUCHEROS+)		
2460711.2552	-79.62	0.54	TIC 21673730 (MUSICOS)			2460516.5284	-1.13	1.10
2460711.2552	93.41	0.45	2460830.4102	-47.81	1.90	2460518.5704	-1.05	0.46
2460711.2552	22.54	0.70	2460833.4144	-17.65	1.90	2460520.4925	-0.38	1.10
2460715.3399	-65.63	0.52	2460836.4197	11.43	2.00	2460569.5185	0.01	0.02
2460715.3399	85.20	0.50	2460838.4285	10.35	2.30	TIC 174214184 (PUCHEROS+)		
2460715.3399	10.80	1.30	2460848.4137	49.56	2.00	2460517.5187	-24.26	2.30
2460716.2484	-57.77	0.58	2460849.3998	-10.80	1.50	2460519.5826	-24.39	1.90
2460716.2484	79.01	0.48	TIC 31623275 (PUCHEROS+)			2460530.5308	-25.99	0.90
2460716.2484	9.30	1.40	2460495.8278	0.00	0.00	2460534.5693	-22.23	1.90
2460716.2767	-54.21	0.60	2460499.8362	-27.98	1.70	2460545.5152	-25.46	1.30
2460716.2767	75.53	0.51	2460532.6537	-0.38	1.30	2460547.5421	-26.55	0.91
2460716.2767	10.53	1.40	2460536.5226	-28.80	1.50	2460559.5006	-25.08	1.10
2460722.2462	-59.70	0.37	2460543.7584	-4.60	1.70	2460567.5070	-26.58	1.20
2460722.2462	92.21	0.52	2460545.7314	-20.64	2.40	TIC 184607315 (OES)		
2460722.2462	-4.34	1.10	2460573.5987	-25.18	1.20	2460559.4828	0.00	0.00
2460722.2746	-60.84	0.41	2460574.6109	-12.44	1.70	2460576.5119	-5.00	0.37
2460722.2746	93.45	0.53	TIC 61449214 (PUCHEROS+)			2460583.4688	-7.62	0.44
2460722.2746	-3.11	1.20	2460516.5476	-0.78	1.90	2460663.2956	-42.26	0.39
2460726.2386	1.62	0.48	2460518.5898	-0.55	2.10	2460672.2996	-45.16	0.40
2460726.2386	37.86	0.65	2460520.5145	-1.60	3.10	2460673.3315	-45.55	0.43
2460726.2386	-7.23	1.40	2460531.5495	-0.01	2.40	2460674.3367	-45.69	0.42
TIC 14400891 (MUSICOS)			2460565.5034	-0.22	1.40	2460683.3312	-48.13	0.50
2460712.3107	6.83	0.13	2460572.5242	-0.33	1.90	TIC 205913291 (PUCHEROS+)		
2460717.4384	-44.28	0.40	2460573.5141	0.84	1.90	2460514.5770	-2.33	0.87
2460717.4384	71.81	0.52	2460574.4891	-0.18	3.30	2460520.5609	-3.28	0.53
2460717.4384	6.65	1.20	2460577.4826	-0.01	0.01	2460530.6331	-5.87	0.79
2460731.5141	-52.44	0.50	TIC 66497441 (PUCHEROS+)			2460544.4944	-6.74	1.50
2460731.5141	104.70	0.90	2460495.9073	30.15	1.80	2460545.6276	-7.30	1.00
TIC 16878120 (OES)			2460499.9357	29.85	0.85	2460556.5585	-0.01	0.00
2460428.4665	3.70	2.90	2460499.9416	30.05	1.20	TIC 212031970 (PUCHEROS+)		
2460429.5872	0.28	2.40	2460518.7049	25.16	1.20	2460520.5389	-81.98	3.20
2460431.4580	1.00	2.90	2460532.6977	19.87	1.30	2460520.5389	76.28	3.70
2460433.4453	0.36	2.90	2460533.7867	18.47	1.20	2460530.6136	-68.60	2.80
2460435.4059	-0.58	0.02	2460543.8289	14.39	4.30	2460530.6136	72.01	4.60
2460511.3557	-9.34	2.60	2460545.8049	14.15	0.84	2460544.4748	-19.78	2.60
2460512.3577	-11.74	2.30	2460558.8243	8.09	1.20	2460544.4748	22.41	4.30
2460520.3164	-11.55	3.00	2460559.8609	6.88	1.10	2460545.5838	-61.35	36.00
2460523.3282	-14.42	0.90	2460569.7355	2.11	1.40	2460545.5838	9.00	4.70
2460526.3264	-14.63	1.60	2460573.6427	1.39	1.00	2460556.5390	-98.69	3.10
2460738.6690	-2.87	4.50	2460575.6316	-0.03	0.31	2460556.5390	93.53	2.90
2460740.6321	12.83	3.70	TIC 84756974 (PUCHEROS+)			2460566.5810	-119.34	3.80
2460743.6360	-6.03	2.40	2460514.5570	0.00	0.00	2460566.5810	112.84	5.00
2460746.5634	11.24	3.60	2460518.6109	-0.60	5.10			

Table B.1. continued

HJD	RV (km s^{-1})	err (km s^{-1})	HJD	RV (km s^{-1})	err (km s^{-1})	HJD	RV (km s^{-1})	err (km s^{-1})
TIC 218160121 (PUCHEROS+)			TIC 293069615 (PUCHEROS+)			TIC 347699402 (MUSICOS)		
2460439.8756	-77.89	12.00	2460519.6869	79.76	1.10	2460879.3642	-0.65	0.87
2460440.8527	-82.57	15.00	2460520.5922	-68.54	1.80	TIC 351532879 (PUCHEROS+)		
2460499.7717	-40.08	14.00	2460520.5922	62.77	1.80	2460499.8550	-78.48	2.60
2460535.5536	-47.99	15.00	2460530.5923	-55.96	1.20	2460499.8550	90.35	3.20
2460545.6815	-48.99	15.00	2460530.5923	51.90	1.30	2460500.8083	-0.31	1.50
2460555.5300	-48.12	12.00	2460535.5288	-45.83	1.10	2460510.6697	-81.39	4.10
2460573.5580	-47.70	0.54	2460535.5288	38.60	1.30	2460510.6697	80.36	2.10
TIC 220485766 (PUCHEROS+)			2460545.6450	-52.79	1.00	2460513.8270	-40.34	6.20
2460495.8828	-28.20	0.97	2460545.6450	48.05	1.10	2460513.8270	42.89	2.80
2460499.8788	10.26	1.20	2460566.6023	-36.88	1.00	2460518.6550	-95.84	4.00
2460500.8955	-21.63	2.10	2460566.6023	31.15	1.20	2460518.6550	90.59	2.20
2460500.9133	-20.99	1.80	2460574.5365	-48.82	0.91	2460531.6876	2.83	4.80
2460543.8038	-27.22	1.30	2460574.5365	43.80	1.00	2460545.6633	-75.33	3.20
2460545.7649	-10.76	1.00	TIC 302581695 (OES)			2460545.6633	86.48	3.80
2460560.7470	3.02	0.67	2460428.3639	0.00	0.00	2460556.6051	4.77	0.93
2460565.7252	-8.31	1.40	2460429.4146	-11.76	1.50	2460568.7067	6.72	1.30
2460567.8044	-27.52	1.10	2460430.3624	1.47	1.20	TIC 419610625 (PUCHEROS+)		
2460568.7751	-0.10	0.01	2460431.3573	-15.86	1.40	2460499.8637	-24.37	0.24
2460575.6070	-27.02	2.10	2460433.3454	-15.03	1.50	2460500.8190	15.06	0.31
TIC 226037840 (PUCHEROS+)			2460435.3046	-17.48	2.10	2460510.6786	-22.14	0.35
2460517.5634	-11.30	7.20	2460436.3112	1.18	2.10	2460518.6633	-6.01	0.27
2460517.5831	-30.85	16.00	2460707.5776	-14.95	1.90	2460519.7562	-13.00	0.36
2460519.6531	-2.80	6.00	2460709.3922	-18.26	2.00	2460543.7860	-7.29	0.36
2460545.5686	-2.67	7.80	2460711.2407	-16.08	1.70	2460545.7477	22.26	0.51
2460569.5620	-6.98	5.80	2460715.3252	-20.93	2.40	2460559.6020	21.31	0.27
TIC 257456854 (OES)			2460722.5093	2.28	1.90	2460565.6900	12.13	0.32
2460428.5319	-79.31	0.56	TIC 302581695 (MUSICOS)			2460568.7185	-0.04	0.00
2460428.5319	60.97	0.62	2460712.2732	-2.66	4.80	TIC 444577764 (PUCHEROS+)		
2460430.5294	-62.31	0.37	2460715.4068	-23.48	4.30	2460554.5447	-15.75	6.00
2460430.5294	44.05	0.46	2460717.5150	-23.09	3.60	2460564.5294	-0.08	0.01
2460431.4949	-38.80	0.50	2460728.4267	-2.92	4.70	TIC 448876509 (PUCHEROS+)		
2460431.4949	16.13	0.45	TIC 302666414 (OES)			2460516.5070	0.00	0.00
2460433.4819	-31.81	0.43	2460431.4031	0.00	0.00	2460518.5273	-2.67	0.20
2460433.4819	7.93	0.49	2460433.3905	-28.27	0.15	2460530.4900	-1.63	0.39
2460511.4087	-11.78	0.26	2460435.3505	-14.62	0.35	2460564.5795	-2.26	0.62
2460512.4158	-37.99	0.44	2460436.3573	-32.27	0.22	2460569.4989	-1.21	0.57
2460512.4158	15.77	0.55	2460709.4763	-24.73	0.10	2460570.5614	-2.18	0.26
2460520.3557	-33.48	0.42	2460715.4836	-32.42	0.20			
2460520.3557	8.61	0.42	2460716.5513	-6.25	0.21			
2460523.3679	-75.56	0.59	2460722.3418	-24.76	0.43			
2460523.3679	57.68	0.65	2460722.4848	-19.47	0.20			
2460526.3847	-60.77	0.46	TIC 302666414 (MUSICOS)					
2460526.3847	34.97	0.42	2460712.3473	-31.48	0.43			
2460559.2909	-78.37	0.52	2460715.5680	-31.76	0.46			
2460559.2909	58.25	0.61	2460717.5401	-9.42	0.40			
TIC 257456854 (MUSICOS)			2460728.5046	-29.92	0.32			
2460830.4519	-50.01	0.43	TIC 310932102 (OES)					
2460830.4519	27.37	0.54	2460511.4820	-0.99	0.85			
2460833.4517	-80.00	0.53	2460512.4608	-2.39	0.70			
2460833.4517	53.69	0.49	2460520.3929	-3.28	0.84			
2460835.3559	-40.75	0.51	2460523.4049	-0.02	0.00			
2460835.3559	15.55	0.47	2460856.4279	3.32	1.00			
2460836.3840	-23.39	0.94	2460870.3612	5.39	0.89			
2460836.3840	-4.65	0.49	TIC 310932102 (MUSICOS)					
2460838.3924	-47.68	0.52	2460860.3476	2.81	3.00			
2460838.3924	21.47	0.52	TIC 320692159 (MUSICOS)					
2460848.4524	-55.76	1.00	2460860.3842	-28.37	4.20			
2460848.4524	34.51	1.10	2460860.3842	37.30	5.30			
TIC 279821618 (PUCHEROS+)			2460861.3828	-36.30	4.80			
2460517.5423	4.12	2.90	2460861.3828	45.81	6.10			
2460519.6262	6.55	3.50	TIC 342829903 (PUCHEROS+)					
2460530.5613	8.65	4.50	2460516.4869	-84.93	2.40			
2460545.5437	4.41	6.10	2460516.4869	101.44	2.50			
2460547.5831	6.48	5.60	2460518.4858	6.71	1.40			
2460556.5188	0.05	0.03	2460522.5411	-84.09	7.30			
2460565.5278	2.29	3.70	2460522.5411	105.90	7.60			
2460569.5407	2.71	4.20	2460530.4700	-85.81	2.40			
TIC 292207311 (PUCHEROS+)			2460530.4700	102.88	2.40			
2460517.4984	7.60	1.70	TIC 347699402 (OES)					
2460519.5324	-6.27	1.70	2460511.4242	0.29	0.13			
2460530.5109	-4.66	2.00	2460512.4345	0.12	0.24			
2460558.4734	-3.52	1.50	2460520.3714	-0.89	0.07			
2460566.5308	5.15	3.10	2460523.3835	0.97	0.29			
2460577.5024	-0.03	0.01	2460526.4005	-0.06	0.06			
TIC 293069615 (PUCHEROS+)			2460526.4171	0.02	0.00			
2460514.5269	-84.33	1.40	2460870.5444	0.38	0.12			
2460514.5269	80.98	1.20	TIC 347699402 (MUSICOS)					
2460519.6869	-84.33	1.20	2460859.4025	-0.33	0.72			